

Cite this: *J. Mater. Chem. A*, 2026, **14**, 15275

Boosting CO₂ methanation over Ni-based catalysts via La–Al mixed oxide synergy

R. B. Machado-Silva,^a L. M. Andrés-Olmos,^a N. Kosinov,^b E. J. M. Hensen^b and A. Chica^b *^a

LaAlO₃ demonstrated a pronounced mixed-oxide synergistic effect as a support for Ni-based catalysts in the CO₂ methanation reaction. Catalysts supported on LaAlO₃ exhibited higher CH₄ yields and turnover frequency (TOF) values than those supported on the individual oxides, La₂O₃ and Al₂O₃. This enhanced performance was attributed to the higher density of intermediate-strength basic sites and the lower apparent activation energies associated with the LaAlO₃-supported catalysts. Among the tested formulations, the 15 wt% Ni catalyst on LaAlO₃ (15Ni/LaAlO₃) showed the best performance, achieving 91% CO₂ conversion and 99% CH₄ selectivity at 350 °C under high space velocity conditions [10 000 mL (g cat·h⁻¹)]. A comprehensive characterization using SEM-TEM, TPR, and H₂-chemisorption, combined with a mechanistic assessment *via* time-resolved *operando* FT-IR spectroscopy, revealed that the catalyst's activity stems from a well-balanced distribution of moderate basic sites and high Ni⁰ surface availability. This combination favors the complete reduction of carbonated intermediates through a hydrogen-assisted associative pathway, with monodentate carbonate and Ni⁰-CO identified as key intermediates. Additionally, 15Ni/LaAlO₃ was evaluated for the first time in biogas upgrading. Using a model sweetened biogas mixture (60% CH₄-40% CO₂), the catalyst produced biomethane with 90.2% CH₄ content after 24 hours of continuous operation, confirming its potential for sustainable energy applications.

Received 4th January 2026
Accepted 1st March 2026

DOI: 10.1039/d6ta00070c

rsc.li/materials-a

1. Introduction

Mixed oxides have emerged as a versatile class of materials whose physicochemical properties often surpass those of their single-oxide counterparts.¹ In this sense, the concept of “mixed-oxide synergy” refers to the cooperative interactions between distinct cations and structural frameworks, which give rise to new functionalities or enhanced performance in comparison with the individual oxides.²

Such synergistic effects can manifest in a wide range of phenomena, including increased thermal stability, improved redox behavior, modified electronic structures, creation of novel active sites, and modification of catalytic properties.^{3–5} Regarding the application in catalysis, several reports have been explored for different reactions, such as N₂O decomposition,⁶ acetic acid steam reforming⁷ and CH₄ dry reforming⁸ reactions. Despite the many processes already investigated, comparatively few studies have focused on the CO₂ methanation reaction, even though it offers significant potential.

CO₂ methanation, also known as the Sabatier reaction, is a suitable approach for hydrogenating CO₂ into CH₄ using H₂ obtained from green sources, such as solar or wind power-driven electrolysis.⁹ At present, with the development of catalytic technologies capable of optimizing Carbon Capture Utilization and Storage (CCUS) processes, this reaction has taken on a relevant scientific prominence with the aim of mitigating the effects of global warming.

In addition, CO₂ methanation plays a key role in biogas upgrading, where the CO₂ fraction present in biogas is converted into CH₄, enabling the production of high-quality biomethane compatible with existing natural gas infrastructure.¹⁰

Due to the kinetic and thermodynamic limitations, this reaction is conducted in the presence of a catalyst to optimize the CO₂ conversion and selectivity toward CH₄.^{11,12} These catalysts consist of metal nanoparticles supported on inorganic support, and there is an ongoing interest in developing stable, cheap, CH₄-selective, and low-temperature-active materials.¹³

Regarding the metallic phase, different transition metals present significant catalytic activity (Ni, Ru, Fe, Co, and Rh).^{14–17} Ni-based catalysts typically exhibit high activity and superior selectivity toward CH₄, while minimizing the formation of undesired by-products, as observed in Fe or Co-based ones. In addition to these catalytic advantages, nickel offers substantially lower cost and greater availability compared to noble

^aInstituto de Tecnología Química (Universitat Politècnica de València-Consejo Superior de Investigaciones Científicas), Avd. de los Naranjos s/n, Valencia 46022, Spain. E-mail: achica@itq.upv.es

^bLaboratory of Inorganic Materials and Catalysis, Department of Chemical Engineering and Chemistry, Eindhoven University of Technology, Helix, STW 3.33, Het Kranenveld 14, AZ 5612, Eindhoven, The Netherlands



metals, making it especially suitable for large-scale and industrial applications without significant concerns related to resource scarcity.¹⁸

As for the support used for the catalysts, the material is critical, as it significantly impacts the material's performance, stability, and activity. Inorganic oxides, such as Al₂O₃,¹⁹ ZrO₂,²⁰ TiO₂,²¹ and other types of porous materials, such as zeolites,²² MOF's,²³ sepiolite,²⁴ and todorokite,²⁵ have already been described in the literature as support for this reaction. Despite the study of various oxides as supports, the synergistic effect of mixed oxides has not been widely explored, particularly for this reaction.

Thus, in this study, a mixed oxide, lanthanum aluminate (LaAlO₃), was selected for the analysis and development of novel Ni-based catalysts for the CO₂ methanation reaction. This material has also been extensively investigated as a catalyst support due to its high-temperature stability, unique electronic properties, and capability to stabilize metal nanoparticles.^{26–28} Notable catalytic applications include their use in methane oxidative coupling, steam reforming of hydrocarbons,²⁹ nitrogen monoxide reduction,³⁰ preferential CO oxidation (CO-PROX),³¹ and soot combustion processes.³²

In light of the current state of knowledge, where no previous research has addressed the potential synergistic contribution of the mixed-metal structure of LaAlO₃ to the CO₂ methanation reaction, this study was undertaken. The strategy adopted comprised two main stages. First, LaAlO₃-supported catalysts were evaluated in comparison with Al₂O₃ and La₂O₃ counterparts. A multi-technique characterization protocol was applied, including XRD, N₂-physisorption, ICP, TEM, H₂-chemisorption, H₂-TPR, CO₂-TPD-MS, and *operando* FT-IR analyses, in order to examine how variations in Ni⁰ particle size and available surface area relate to modifications in the concentration of intermediate-strength basic sites, CO₂ adsorption properties, and their overall impact on the catalytic process.

Despite extensive research efforts, the mechanistic pathway of CO₂ methanation remains a matter of debate, since a universal agreement on the reaction mechanism has not been reached.³³ Current evidence suggests that basic sites of intermediate strength are involved in CO₂ activation and the generation of reaction intermediates such as Ni⁰-CO, carbonates, and formates. However, their specific mechanistic function still requires deeper investigation.³⁴

To provide further insights, we implemented time-resolved *operando* FT-IR spectroscopy following established procedures from our research group.^{35–37} When these results were interpreted together with kinetic measurements and CO₂-TPD-MS experiments, it became possible to propose new hypotheses concerning the mechanistic participation of basic sites in this family of catalytic systems.

Finally, in the second phase, after thorough characterization of the mixed-oxide synergy, nickel loading was optimized to achieve a novel real-life application. Then, we report for the first time the application of a Ni-based catalyst supported on LaAlO₃ in biogas upgrade by employing the CO₂ methanation reaction to increase the CH₄ content in an emulated sweetened biogas

sample, thereby checking the feasibility of upgrading the sample to renewable natural gas levels.

2. Experimental methodology

2.1 Preparation of catalysts

Commercially available La₂O₃ and Al₂O₃ supports (Sigma-Aldrich) were used for the synthesis of the corresponding supported catalysts. The Al₂O₃ employed was the α -phase material, selected due to its surface area being comparable to that of the other supports. La₂O₃ was pre.

LaAlO₃ was produced *via* the Pechini sol-gel method, as previously reported in the literature.³⁸

For the synthesis, La(NO₃)₃·6H₂O and Al(NO₃)₃·9H₂O were dissolved in 300 mL of isopropanol under vigorous stirring at 60 °C for 30 minutes, maintaining a La concentration of 0.39 mol L⁻¹. Subsequently, 200 mL of polyethylene glycol was added dropwise at 2.25 mL min⁻¹, while stirring continued for an additional 30 minutes. The temperature was then raised to 80 °C for 1 hour to promote isopropanol evaporation. The resulting precursor was calcined in air at 1050 °C for 4 hours.

Two distinct Ni-based catalyst series were prepared. The first group was obtained by incipient wetness impregnation (IWI), employing Ni(NO₃)₂·6H₂O as the metal precursor, followed by calcination at 450 °C for 3 hours. These materials were designated as xNi/support, where *x* corresponds to the nominal Ni loading in weight percent.

The second preparation strategy was based on the ex-solution approach. A Ni-doped LaAlO₃ perovskite containing 5 wt% Ni (denominated 5NiLaAlO₃-ex) was synthesized using the same method described for LaAlO₃, but replacing the precursor mixture with Ni(NO₃)₂·6H₂O, Al(NO₃)₃·9H₂O, and La(NO₃)₃·6H₂O in the appropriate stoichiometry. For both families, reduced forms of the catalysts were generated by treatment under a 150 mL min⁻¹ H₂ flow at 450 °C (heating rate of 10 °C min⁻¹), and the reduced materials were denoted with the suffix “_R”.

2.2 Catalyst characterization

X-ray diffraction patterns were recorded using a PANalytical CUBIX diffractometer operating at 40 kV and 30 mA with $\lambda = 1.5418$ Å. Data were collected in the 2θ range of 10–90° at a scanning speed of 4.5° min⁻¹.

Textural analysis was performed by N₂ physisorption at –196 °C using a Micromeritics Quantachrome ASAP 2020 instrument. BET, BJH, and t-plot methods were applied to determine surface area and micro/mesopore volumes.

Transmission electron microscopy was carried out using a JEOL JEM-2100F microscope operating at 200 kV to determine the Ni⁰ particle size distribution. Prior to analysis, samples were reduced at 450 °C under H₂ flow (150 mL min⁻¹) for 2 hours. The morphology of the solids was additionally examined using a field-emission scanning electron microscope (FESEM, Zeiss Ultra 55).

Metal loading was quantified by inductively coupled plasma atomic emission spectroscopy (ICP-OES) using a Varian 715-ES



instrument (Agilent, Santa Clara, CA, USA). Samples were digested by treating 50 mg of catalyst with 10 mL of 50 wt% H₃PO₂ (Sigma-Aldrich) and 10 mL of an HF:HNO₃:HCl mixture (1 : 1 : 3), prepared from commercial reagents.

H₂-temperature-programmed reduction (H₂-TPR) analyses were performed using a Micromeritics Autochem 2910 system equipped with a thermal conductivity detector. A total of 75 mg of sample was pretreated in Ar for 15 min, then heated up to 900 °C under a 10 vol% H₂ in Ar flow. The reducible fraction of Ni species was calculated following procedures reported by our research group.³⁹

CO₂-temperature programmed desorption coupled with mass spectrometry (CO₂-TPD-MS) was conducted using 100 mg of catalyst. Samples were reduced under H₂ flow (150 mL min⁻¹) at 450 °C for 2 hours, followed by saturation with CO₂ pulses at 40 °C. Desorption was carried out up to 900 °C (10 °C min⁻¹). Evolved CO₂ was monitored with a Balzers Prisma QME 200 quadrupole mass spectrometer by tracking the *m/z* 44 signal. Quantification was referenced to a CeO₂ standard.

H₂-chemisorption was performed in a Quantachrome Autosorb-1C instrument using a methodology previously reported by our group.⁴⁰ Approximately 250 mg of sieved catalyst (0.2–0.4 mm) was reduced at 450 °C under H₂ flow, followed by adsorption–desorption cycles. The number of accessible Ni sites per gram of catalyst, $\bar{N}_{\text{available,Ni}}$, was determined assuming a stoichiometric ratio H/Ni = 1 and applying the calculations previously described.⁴¹

Operando transmission FT-IR experiments were carried out using a custom-designed cell attached to a Nicolet 6700 spectrometer, following an adapted methodology from our earlier work.²⁵ Self-supported wafers (10 μm thick) were prepared from dry catalyst powder. The material was reduced at 450 °C for 1 hour under He, cooled to 250 °C, and exposed for 10 min to a CO₂/He gas mixture (He:CO₂ = 5 molar ratio, total flow 30 mL min⁻¹), with spectra collected every 30 seconds at 2 cm⁻¹ resolution with 32 scans. Afterward, CO₂ was removed and replaced by a H₂/He mixture (He:H₂ = 4 molar ratio, 30 mL min⁻¹), maintaining the same acquisition frequency.

2.3 CO₂ methanation and biogas upgrading tests

Catalytic activity measurements for CO₂ methanation were performed in a continuous-flow fixed-bed reactor operating at atmospheric pressure. The reaction temperature ranged from 250 °C to 450 °C, at 1 atm, with a WHSV = 38 000 mL·(g_{cat}·h)⁻¹. A total of 0.350 g of catalyst, with pellet sizes ranging from 0.2 to 0.4 mm, was diluted with SiC to maintain a constant bed volume of 5 mL.

Prior to the reaction, the catalysts were reduced *in situ* by flowing H₂ at 450 °C using a heating rate of 10 °C min⁻¹. Catalytic experiments were performed with an inlet gas feed of 250 mL min⁻¹ composed of CO₂, H₂, and N₂ in a 18 : 72 : 10 molar ratio, where N₂ was used as an internal standard for quantification. The reactor outlet composition was analyzed online using a Varian 3800 gas chromatograph (Agilent, Santa Clara, CA, USA) equipped with a HayeSep Q column and both TCD and FID detectors. Each temperature point was measured

in triplicate, and the results presented represent the corresponding average. Only CH₄, CO, and H₂O were detected throughout the entire range of experimental conditions studied.

CO₂ conversion (X_{CO_2}), methane selectivity (S_{CH_4}), methane yield (Y_{CH_4}), and turnover frequency for CH₄ production (TOF) were determined following the equations below:

$$X_{\text{CO}_2} = \frac{\dot{n}_{\text{CO}_2,\text{in}} - \dot{n}_{\text{CO}_2,\text{out}}}{\dot{n}_{\text{CO}_2,\text{in}}} \times 100\% \quad (1)$$

$$S_{\text{CH}_4} = \frac{\dot{n}_{\text{CH}_4,\text{out}}}{\dot{n}_{\text{CH}_4,\text{out}} + \dot{n}_{\text{CO},\text{out}}} \times 100\% \quad (2)$$

$$Y_{\text{CH}_4} = \frac{X_{\text{CH}_4} \times Y_{\text{CH}_4\%}}{100} \quad (3)$$

$$\text{TOF} = \frac{\dot{n}_{\text{CH}_4,\text{out}}}{0.350 \text{ g} \times \bar{N}_{\text{available,Ni}}} \quad (4)$$

where \dot{n}_{CO_2} , \dot{n}_{CH_4} and \dot{n}_{CO} are the flows, in mol h⁻¹, of CO₂, CH₄ and CO, respectively, $\bar{N}_{\text{available,Ni}}$ is the molar amount of Ni sites per catalyst gram calculated by the H₂-chemisorption analyses, and the subscripts in and out refer to the input and output flow of the reactor, respectively.

Kinetic measurements were performed in the temperature range of 250 to 270 °C, where the CO₂ conversion was maintained below 10% to ensure operation in the kinetic regime. The apparent activation energy for methane formation (E_{a,CH_4}) was determined from the slope of Arrhenius plots constructed from these data.

To evaluate performance under conditions relevant to biogas upgrading, catalytic tests were conducted using the best-performing formulation, 15Ni/LaAlO₃, in addition to the initial tests. Contact time (τ) optimization was carried out by varying the WHSV between 6000 and 38 000 mL·(g_{cat}·h)⁻¹ at 320 °C.

Subsequent biogas upgrading trials were executed under similar operating conditions, but with an inlet gas mixture representative of sweetened synthetic biogas. The feed consisted of CO₂, H₂, N₂, and CH₄ flows of 45, 180, 25, and 67.5 mL min⁻¹, respectively, resulting in a composition of 60% CH₄ and 40% CO₂.⁴² Catalyst stability was monitored for 24 hours under these conditions, with outlet gas composition recorded every 24.7 min. The material recovered after the stability evaluation is labeled with the suffix “_ST”, corresponding to “Stability Test”.

3. Results and discussions

3.1 Characterization results

To investigate the influence of the mixed-oxide effect, three supports were selected for initial evaluation: La₂O₃, Al₂O₃, and LaAlO₃. The corresponding 5 wt% Ni catalysts prepared *via* incipient wetness impregnation were characterized by XRD (Fig. S1 and S2). The diffractograms of La₂O₃ show its characteristic reflections (JCPDS 05-0602), together with additional



peaks attributed to $\text{La}(\text{OH})_3$ (JCPDS 036-1481), which commonly forms due to the strong hydrophilic nature of lanthanum oxide surfaces.⁴³

For the Al_2O_3 -based sample, diffraction features corresponding to crystalline $\alpha\text{-Al}_2\text{O}_3$ were detected (JCPDS 036-1481). In the case of LaAlO_3 synthesized using the Pechini method, a well-defined crystalline perovskite structure was observed. Characteristic reflections appeared at 2θ values of 23.45° (012), 33.38° (110), 41.19° (202), 47.96° (024), 54.02° (116), 59.79° (018), and 70.23° (208), which match the reference pattern for LaAlO_3 (JCPDS 31-0022). The absence of diffraction peaks associated with La_2O_3 or Al_2O_3 indicates complete integration of La^{3+} and Al^{3+} ions into the perovskite lattice under the selected synthesis conditions, a conclusion consistent with ICP results (Table S1).

Thermal analysis of the impregnated materials confirmed the successful decomposition of $\text{Ni}(\text{NO}_3)_2$ into NiO below the selected calcination temperature of 450°C (TG-DSC, Fig. S3).⁴⁴ Furthermore, ICP-OES quantification (Table S1) showed that the measured Ni contents were in close agreement with the nominal values, confirming efficient metal incorporation.

SEM and TEM analyses (Fig. 1, S4 and S5) revealed that LaAlO_3 forms rod-like nanoparticles with lengths ranging from

approximately 100 to 500 nm, consistent with previous reports employing similar synthesis routes.⁴⁵

For Ni-impregnated LaAlO_3 materials, XRD patterns exhibited reflections at $2\theta = 37.40^\circ$ and 43.46° attributed to NiO (JCPDS 47-1049), with intensity increasing as Ni loading increased, indicating a progressive presence of surface NiO species (Fig. S6). TEM-EDS mapping further verified the localization of NiO on the perovskite surface (Fig. S5). After H_2 reduction, the NiO reflections disappeared, and new peaks associated with metallic Ni^0 emerged (JCPDS 01-045-1027) (Fig. S7 and S8). Consistent with particle growth behavior, higher Ni loadings resulted in larger average Ni^0 particle sizes, as determined from TEM size distribution analyses (Fig. S9).

For the sample in which Ni was incorporated into the aluminate phase by coprecipitation to generate a Ni^0 active phase through ex-solution ($5\text{NiLaAlO}_3\text{-ex}$), no NiO reflections were detected in the XRD pattern (Fig. S6). Instead, a slight shift of the LaAlO_3 peaks toward lower 2θ values was observed. This behavior is attributed to the presence of Ni^{3+} ions substituting Al^{3+} in the perovskite lattice, as previously reported by Gibert.⁴⁶ Since Ni^{3+} (ionic radius 60 pm) is slightly larger than Al^{3+} (ionic radius 50 pm), the substitution results in lattice expansion, which explains the shift in Bragg peak positions.

After the reduction treatment, the ex-solved $5\text{NiLaAlO}_3\text{-ex}_R$ sample exhibits smaller Ni^0 crystallites compared with its impregnated counterpart, as confirmed by TEM images. This effect is attributed to the well-dispersed metallic nanoparticles emerging from the perovskite lattice upon reduction, in agreement with the observations by Oliveira *et al.*⁴⁷ The formation of the Ni^0 phase is further confirmed by XRD results (Fig. S8).

Textural properties determined by N_2 adsorption-desorption isotherms (Table 1) show that the BET surface area (S_{BET}) of the synthesized LaAlO_3 is $15\text{ m}^2\text{ g}^{-1}$, consistent with previously reported values.³⁸ The S_{BET} values measured for the commercial La_2O_3 and $\alpha\text{-Al}_2\text{O}_3$ samples were similarly aligned with those previously reported.^{48,49} $\alpha\text{-Al}_2\text{O}_3$ was intentionally selected due to its low surface area, similar to that of La_2O_3 and LaAlO_3 , to maintain comparable Ni particle sizes across all catalysts and therefore enable the direct evaluation of the support effect on catalytic performance.

After Ni deposition, a slight decrease in S_{BET} is observed for all supports. This behavior can be attributed to two distinct contributions. First, NiO crystallites partially block the mesopores of the supports, which reduces the mesopore surface area. Second, the addition of a lower surface area phase (NiO) results in a dilution effect that decreases the surface area per gram of catalyst,⁵⁰ especially in higher Ni loading samples (Table 1).

H_2 -TPR results (Fig. 2) indicate that catalysts prepared on different supports exhibit multiple reduction events between 200 and 500°C . The low-temperature peaks correspond to the reduction of NiO weakly interacting with the support, while the intermediate-temperature peaks reflect NiO species more strongly interacting with the surface.⁵¹ Small peaks at higher temperatures are attributed to Ni^{2+} species incorporated into spinel-type phases such as NiAl_2O_4 and NiLa_2O_4 , which are more difficult to reduce due to the strong metal-lattice interaction.⁵² The temperature at which the highest-

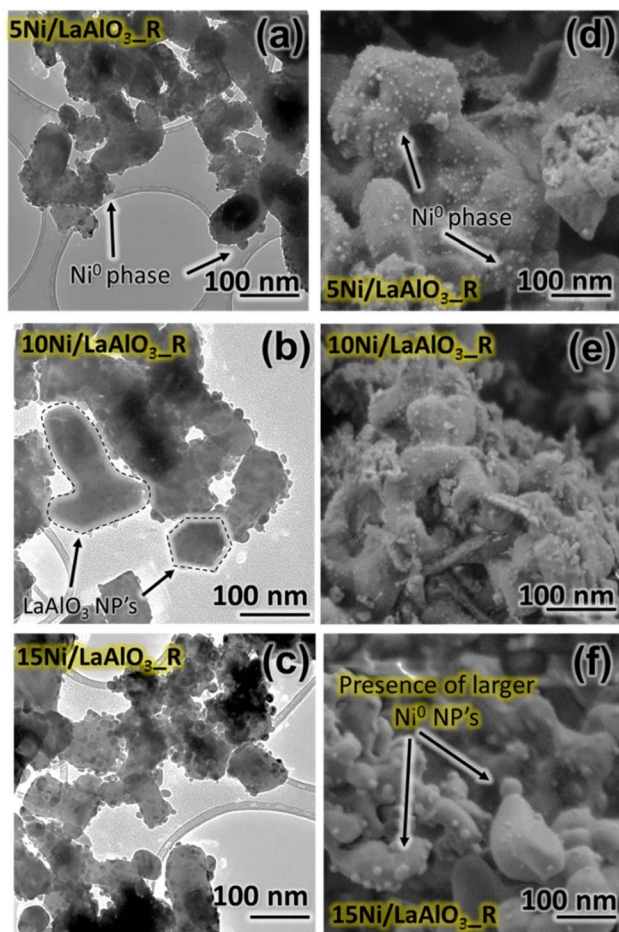


Fig. 1 TEM and SEM characterization of reduced catalysts containing different Ni amounts: $5\text{Ni/LaAlO}_3\text{-R}$ (a) TEM (d) SEM, $10\text{Ni/LaAlO}_3\text{-R}$ (b) TEM (e) SEM, and $15\text{Ni/LaAlO}_3\text{-R}$ (c) TEM (f) SEM.



Table 1 Surface properties: BET surface area (S_{BET}), t-plot mesopore area (S_{MESO}), t-plot mesopore volume (V_{MESO}), Ni^0 metallic surface area (S_{Ni}), Ni^0 average crystallite size, (D_{Ni}), and molar H_2 monolayer uptake

Sample	S_{BET}^a	S_{MESO}^a	V_{MESO}^a	S_{Ni}^b	D_{Ni}^b (nm)	H_2 uptake ^b ($\mu\text{mol g}^{-1}$)
La_2O_3	13	11.7	0.030	—	—	—
5Ni/ La_2O_3	10	9.2	0.027	3.0	10	43.6
Al_2O_3	15	14.9	0.041	—	—	—
5Ni/ Al_2O_3	11	9.6	0.035	3.7	11	54.3
LaAlO_3	15	11.6	0.032	—	—	—
5Ni LaAlO_3 -ex	14	10.9	0.030	3.2	8	40.0
5Ni/ LaAlO_3	15	11.3	0.026	3.4	10	48.3
10Ni/ LaAlO_3	10	9.5	0.023	5.7	12	73.2
15Ni/ LaAlO_3	7	8	0.021	6.2	16	78.8

^a Determined by N_2 -adsorption-desorption technique. ^b Determined by H_2 -chemisorption technique.

temperature peak appears follows the order: Al_2O_3 (663 °C) < LaAlO_3 (750 °C) < La_2O_3 (799 °C). This trend correlates with differences in oxophilicity, since Al interacts more strongly with oxygen than La due to higher polarizability, while LaAlO_3 displays an intermediate behavior.⁵³

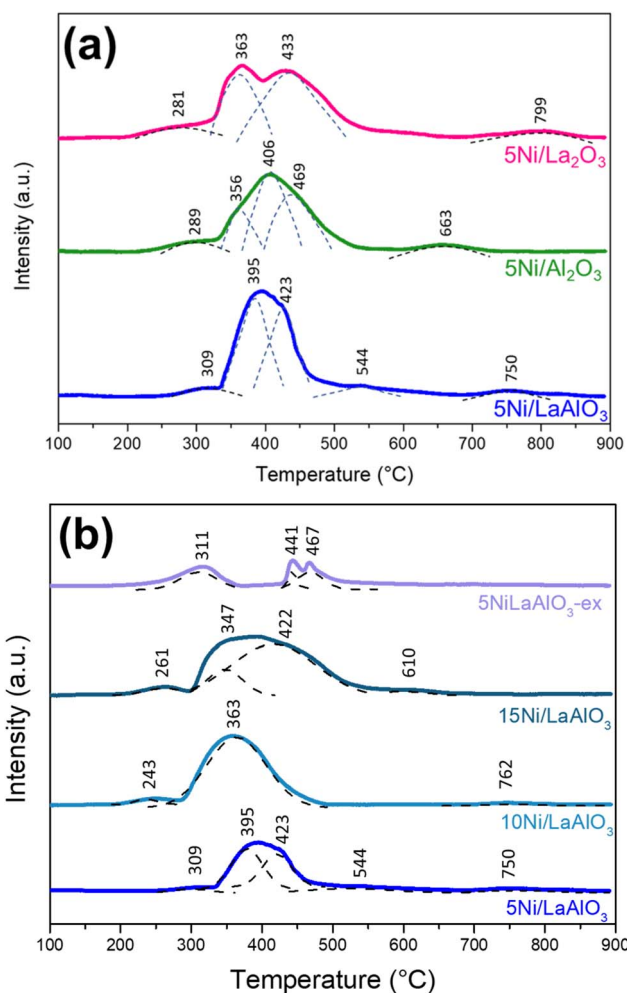


Fig. 2 Hydrogen temperature-programmed reduction profiles for (a) catalysts supported on different oxides and (b) samples with different nickel concentrations. Reduction peak temperatures are provided adjacent to each signal.

For the LaAlO_3 -supported catalysts prepared by impregnation, an increase in Ni loading results in a larger reduction peak area, which is expected due to the higher content of reducible Ni^{2+} species. Increasing the metallic loading also shifts the main reduction peak to lower temperatures: 5Ni/ LaAlO_3 (380 °C) > 10Ni/ LaAlO_3 (363 °C) > 15Ni/ LaAlO_3 (347 °C). This shift is related to the larger crystallite sizes and weaker interactions with the support at higher metal contents, as reported by Singha *et al.*⁵⁴ Additionally, broader peaks are observed for higher Ni loadings, which is attributed to a wider crystallite size distribution (Fig. S9) and a broader range of metal-support interaction strengths.

As previously discussed, the 5Ni LaAlO_3 -ex catalyst exhibits a distinct reduction behavior compared with the materials prepared by impregnation. The first reduction event at 311 °C corresponds to the transition of Ni^{3+} to Ni^{2+} , accompanied by the formation of La_2NiO_5 and La_2NiO_4 phases.^{47,55} The subsequent peaks at 441 and 467 °C are associated with the reduction of Ni^{2+} to Ni^0 , occurring in two steps due to differences in the interaction strength of Ni^{2+} species embedded in the perovskite lattice.

H_2 -chemisorption measurements (Table 1) show that the metallic surface area (S_{Ni}) of the 5 wt% Ni catalysts supported on the different oxides has a comparable magnitude, with Ni^0 dispersion and average crystallite size (D_{Ni}) exhibiting a similar trend. The 5Ni/ Al_2O_3 sample displays slightly higher H_2 uptake values, which may be associated with the amphoteric character of Al_2O_3 that provides a greater concentration of surface acid sites capable of stabilizing hydrogen atoms through spillover phenomena.⁵⁶

In contrast, 5Ni LaAlO_3 -ex presents a slightly lower S_{Ni} and H_2 uptake in comparison to 5Ni/ LaAlO_3 , since a fraction of Ni remains incorporated within the crystal lattice, reducing the amount of accessible metallic Ni^0 sites on the surface.

The CO_2 -TPD profiles obtained for the pure supports were evaluated considering three characteristic desorption temperature regions: low (50 to 150 °C), intermediate (150 to 400 °C), and high (400 to 900 °C), corresponding to weak, moderate, and strong basic sites.⁴³, respectively (Fig. 3). The results (Table S2) show that LaAlO_3 exhibits the highest total CO_2 uptake among the supports examined, followed by La_2O_3 and Al_2O_3 .



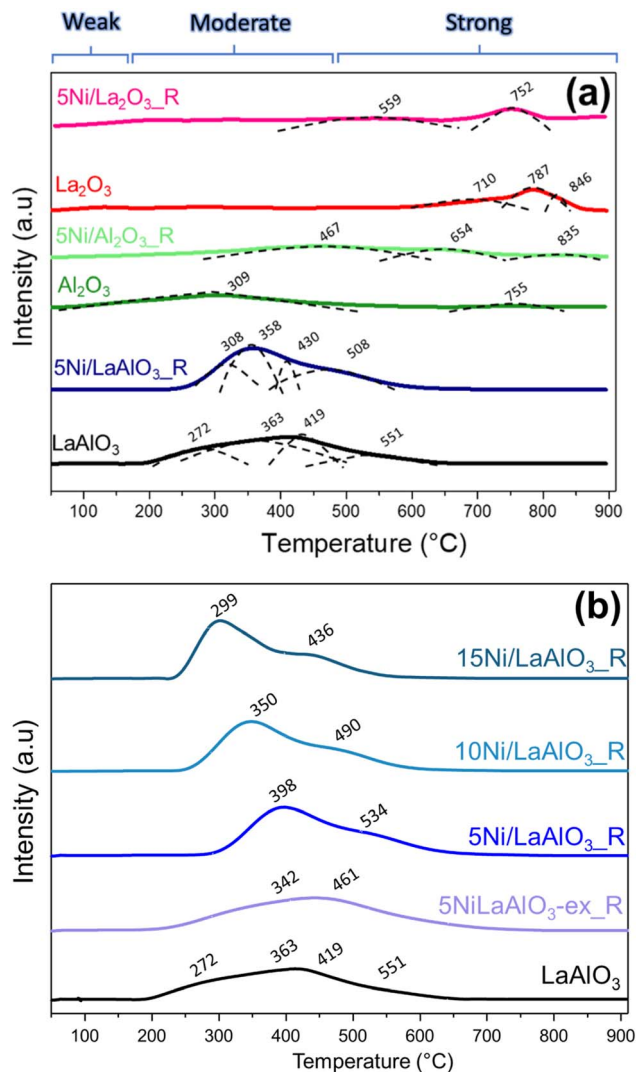


Fig. 3 CO₂-TPD-MS results for (a) supports and (b) catalysts with varying Ni loadings, with desorption event temperatures displayed beside each peak.

Regarding the distribution of basic site strengths, LaAlO₃ also shows the largest contribution of intermediate basic sites (B_{CO_2}), characterized by desorption maxima centered at 363 °C and 419 °C. In contrast, La₂O₃ displays its most intense peak at significantly higher temperature (787 °C), while Al₂O₃ presents a predominant desorption signal at a lower temperature (309 °C).

The intense peaks in the high-temperature region for La₂O₃ (710, 787, and 846 °C) are attributed to the formation of stable La₂O₂CO₃ species [65]. This behavior has been linked to the suppression of carbon deposition in catalysts used for methane dry reforming.⁵⁷ On the other hand, Al₂O₃ does not form oxo-carbonate species, and CO₂ adsorption occurs mainly on surface hydroxyl and oxide groups that decompose at lower temperatures, reflected by the peak centered at 309 °C.⁵⁸

For LaAlO₃, intermediate basicity behavior is observed. The coexistence of Al³⁺ and La³⁺ surface sites promotes significant CO₂ uptake through La₂O₂CO₃ formation and interactions with

surface oxide/hydroxide groups, while the presence of Al³⁺ facilitates CO₂ desorption, shifting the main desorption peak to lower temperatures compared with La₂O₃.

Four resolved desorption features at 272, 363, 419, and 551 °C correspond to distinct carbonate coordination environments.⁵⁹ The formation and reactivity of these carbonate species toward methanation will be further confirmed by *operando* FT-IR results.

It is important to emphasize that the CO₂-TPD-MS results show a clear increase in the amount of CO₂ adsorbed after the introduction of the metallic Ni⁰ phase onto the supports, a trend consistently observed for all three materials (Table S2). Additionally, as the Ni loading increases, the total CO₂ adsorption also rises, as seen in the LaAlO₃-supported catalyst series (Table S2). This enhancement can be attributed to the formation of Ni-carbonyl species, which result from the interaction between CO₂ molecules and metallic Ni⁰ sites as previously described.^{60,61} The presence of these carbonyl species will be further confirmed by *in situ* spectroscopic analyses.

Previous studies using phyllosilicates,⁶² SBA-16,⁶³ C₃N₄,⁶⁴ ZrO₂,⁶⁵ and Al₂O₃ (ref. 66) consistently demonstrate that the concentration of moderate basic sites enhances CO₂ conversion

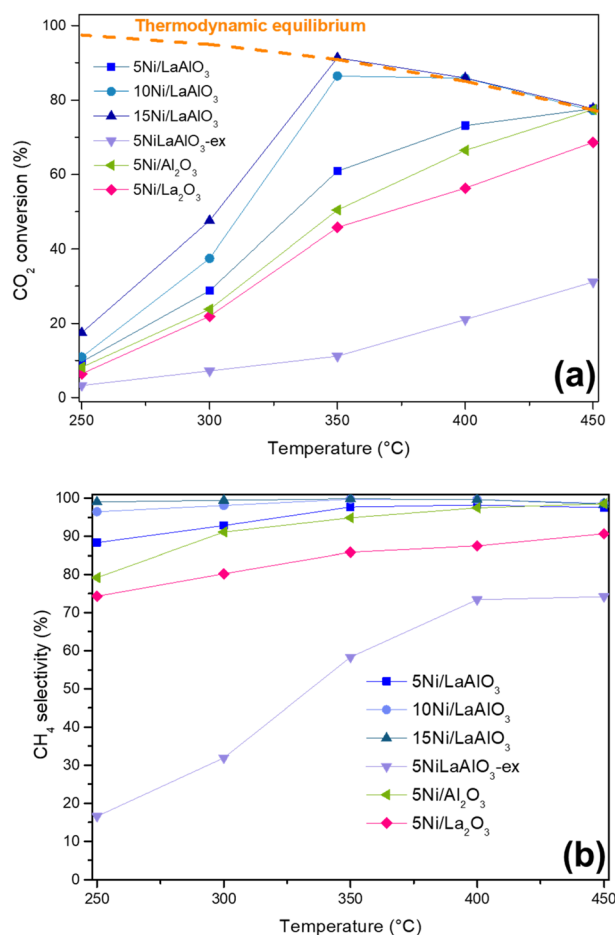


Fig. 4 Catalytic performance in CO₂ methanation: (a) CO₂ conversion and (b) CH₄ selectivity as a function of temperature. Reaction conditions: 250–450 °C, 1 atm, WHSV = 38 000 mL (g_{cat} h)⁻¹, H₂/CO₂ = 4. Equilibrium values were calculated using the DWSIM process simulator.



Table 2 Catalytic performance and selected physicochemical properties of La- and Al-based supported catalysts: CH₄ yield at 250 °C ($Y_{250^\circ\text{C}}$), turnover frequency at 250 °C ($\text{TOF}_{250^\circ\text{C}}$), activation energy for CH₄ formation (E_{a,CH_4}), concentration of moderate basic sites (B_{CO_2}), and average Ni⁰ crystallite size (D_{Ni})

Catalyst	$Y_{250^\circ\text{C}}$ (%)	$\text{TOF}_{250^\circ\text{C}}$ (s ⁻¹)	E_{a,CH_4} ^a	B_{CO_2} ^b	D_{Ni} (nm) ^c
5Ni/La ₂ O ₃	4.7	0.124	89	0.62	11
5Ni/Al ₂ O ₃	6.4	0.131	80	0.91	10
5NiLaAlO ₃ -ex	5.4	0.043	90	2.64	8
5Ni/LaAlO ₃	8.5	0.302	75	3.03	11
10Ni/LaAlO ₃	10.5	0.385	68	3.30	12
15Ni/LaAlO ₃	17.3	0.429	66	3.36	16

^a Obtained from kinetic measurements in the 250–300 °C range. unit: kJ mol⁻¹. ^b Obtained *via* CO₂-TPD-MS analysis. unit: mmol CO₂ g⁻¹. ^c Obtained *via* H₂-chemisorption analysis.

and CH₄ selectivity, which is consistent with the trends observed that will be discussed in the next section.

3.2 CO₂ methanation catalytic tests

3.2.1 Support effect: La₂O₃, Al₂O₃, and LaAlO₃. Catalytic performance was evaluated in terms of CO₂ conversion and CH₄ selectivity (Fig. 4), ensuring a carbon balance within ±5%. Catalysts with higher Ni loading on LaAlO₃ approached equilibrium conversion, as expected for an exergonic process.⁶⁷

At 250 °C, the CO₂ conversion values follows the trend: 5Ni/La₂O₃ < 5Ni/Al₂O₃ < 5Ni/LaAlO₃. This sequence is consistent with TOF values at 250 °C (Table 2) and with the activation energy for CH₄ formation (E_{a,CH_4}) (Fig. 5), confirming the superior intrinsic activity of LaAlO₃-supported catalysts.

Given the comparable S_{Ni} and D_{Ni} values among these catalysts (Table 1), the superior performance of LaAlO₃-supported materials can be attributed to the metal-oxide interaction in this support, which enhances CO₂ adsorption at moderate-strength basic sites and increases the concentration of surface carbonate intermediates. As demonstrated by the mechanistic insights

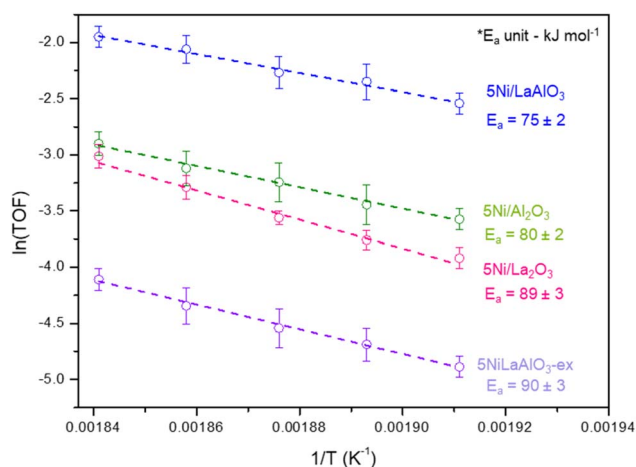


Fig. 5 Temperature-dependent Arrhenius plots for Ni-supported catalysts over various oxides (250–270 °C). Apparent activation energies (E_a) were calculated from the slopes of the corresponding linear fits.

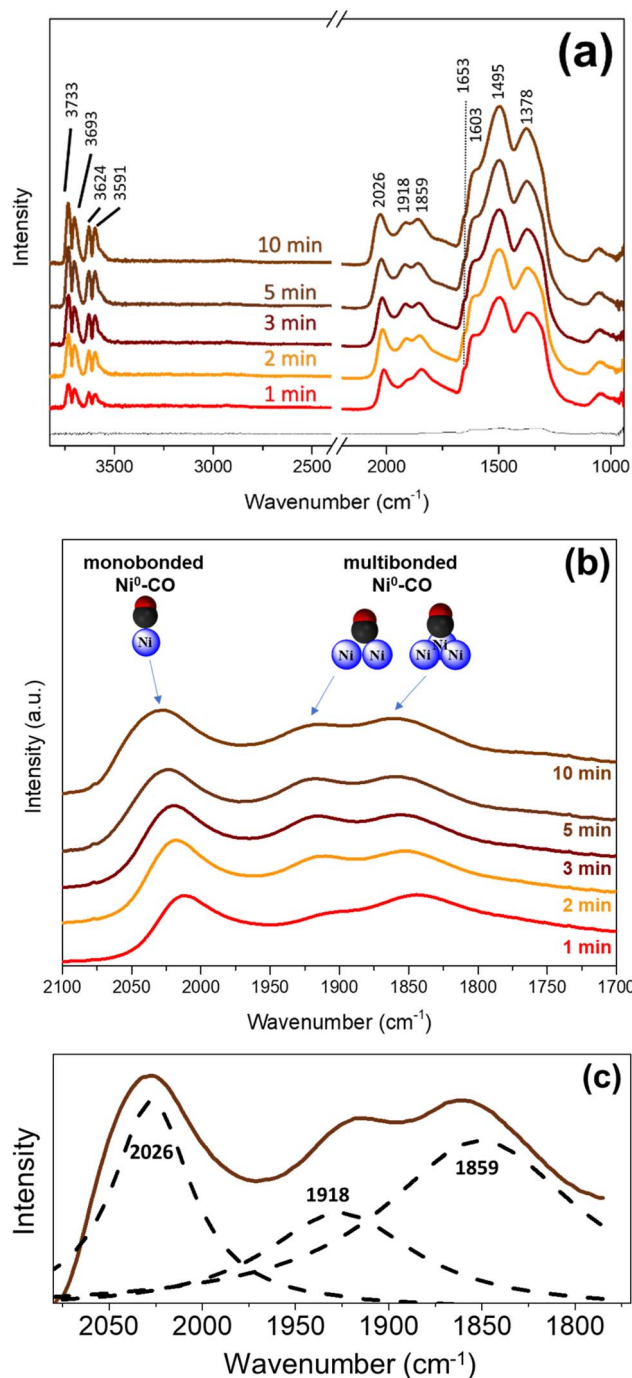


Fig. 6 (a) Transmission FT-IR spectra of 15Ni/LaAlO₃ collected over time during CO₂ adsorption. (b) Enlarged spectral region from 1750 to 2075 cm⁻¹, showing distinct Ni⁰-CO bonding configurations. (c) Deconvolution example for the 10-minute spectrum, illustrating the relative contributions of each Ni⁰-CO species.

from *operando* IR spectroscopy in the next section, these carbonate species actively participate in the reaction pathway; therefore, their higher surface abundance results in increased TOF values.

These findings align with those reported by Italiano *et al.*⁶⁸ who observed elevated TOF values for CO₂ methanation catalysts supported on Y₂O₃, a material characterized by a higher



density of moderate basic sites. Their *operando* analysis results confirmed that on Y_2O_3 , an associative reaction mechanism prevails, with moderate-strength basic sites directly involved in intermediate formation.

3.2.2 Ni loading and catalyst preparation method analysis.

After identifying LaAlO_3 as the most suitable support among the three studied, the influence of Ni loading was investigated. As anticipated, increasing the Ni content enhanced both CO_2 conversion (X_{CO_2}) and CH_4 selectivity (S_{CH_4}), which can be rationalized by two key factors: the Ni^0 particle size and the concentration of intermediate basic sites.

To correlate these catalytic observations with mechanistic insights, the catalyst with the optimal Ni loading, $15\text{Ni}/\text{LaAlO}_3$, was subjected to *operando* FT-IR experiments to probe the intermediates formed during the reaction (Fig. 6) and for the first time, published in the literature. The full dataset is provided in the SI (Fig. S10).

Upon CO_2 introduction, carbonate species were detected, with characteristic bands at 1378, 1495, 1603, and 1653 cm^{-1} (Table S3). Simultaneously, metal-carbonyl species formed with varying coordination environments: linear $\mu_1\text{-CO}$ (2026 cm^{-1}),

bridged $\mu_2\text{-CO}$ (1918 cm^{-1}), and multi-bonded $\mu_3\text{-CO}$ (1859 cm^{-1}), reflecting differences in the electronic density of the C–O bond.⁶⁹

When the CO_2 flow was replaced with H_2 (Fig. 7a), CH_4 formation was observed, as indicated by its characteristic rotovibrational peaks at 3016 and 1302 cm^{-1} .

Modification of the monodentate carbonate bands at 1653 and 1609 cm^{-1} , observed as shoulders to the main bands, occurs upon H_2 introduction, with a decrease in intensity, confirming their active participation in the reaction mechanism, as indicated by the evolution of their normalized areas (Fig. 7b). In contrast, the bidentate carbonate and formate intermediates (1495 and 1378 cm^{-1} , respectively) remain largely unchanged, acting as spectator species. Peaks corresponding to metal-carbonyl groups also diminish, suggesting their involvement in the reaction pathway.

Collectively, these observations indicate that the CO_2 methanation over $15\text{Ni}/\text{LaAlO}_3$ follows a predominantly H-assisted associative mechanism (Fig. S11), in which bicarbonate species are hydrogenated to CH_4 . The concurrent decrease in metal-carbonyl peak intensity also suggests a possible contribution from a dissociative pathway.

Integrating these insights with catalyst performance, the superior activity of higher Ni-loading samples can be attributed to two primary factors: the concentration of intermediate basic sites (B_{CO_2}) and the available metallic surface area (S_{Ni}). To quantify this effect, the ratio $B_{\text{CO}_2}/S_{\text{Ni}}$ was calculated, and its correlation with catalytic activity, expressed as $\ln(\text{TOF})$, was analyzed (Fig. 8).

Regarding the support effect, $5\text{Ni}/\text{La}_2\text{O}_3$, $5\text{Ni}/\text{Al}_2\text{O}_3$, and $5\text{Ni}/\text{LaAlO}_3$ exhibit similar Ni^0 surface areas, with differences primarily arising from their basicity. Previous studies have shown that $\text{Ni}/\text{Al}_2\text{O}_3$ and $\text{Ni}/\text{La}_2\text{O}_3$ also proceed *via* an associative mechanism, where moderate basicity sites facilitate the formation of reactive monodentate carbonate intermediates.^{70,71}

Thus, the mixed-oxide synergy in LaAlO_3 , which enhances the concentration of moderate basic sites, directly promotes the

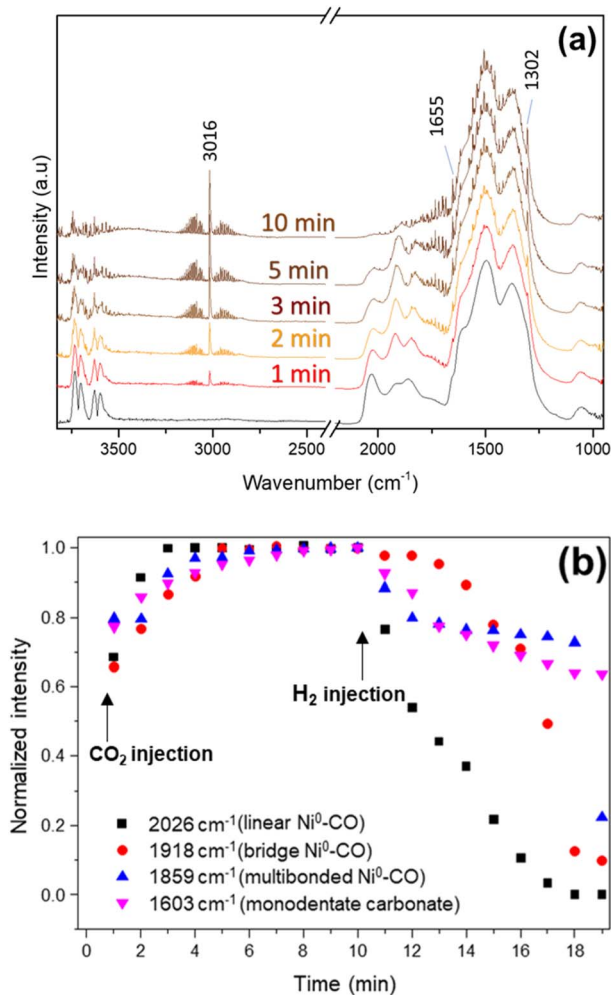


Fig. 7 (a) Evolution of $15\text{Ni}/\text{LaAlO}_3$ surface species monitored by time-resolved *in situ* FT-IR during H_2 flow following CO_2 adsorption. (b) Time profiles of normalized intensities for representative peaks.

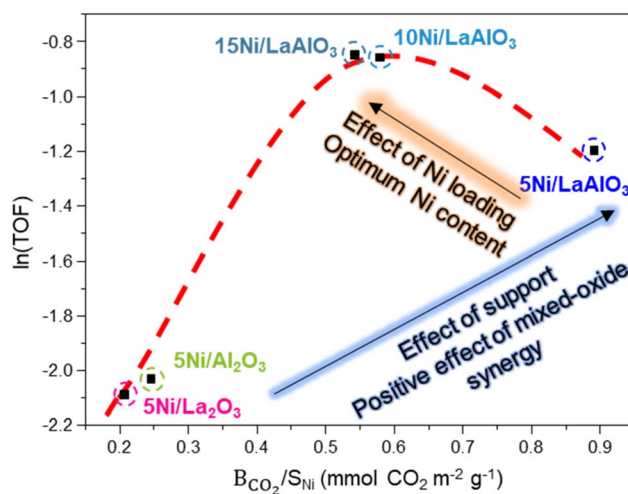


Fig. 8 Impact of the ratio between moderate basic sites concentration, B_{CO_2} , and the available metallic surface area, S_{Ni} , on catalytic performance. The red curve is shown as a visual guide.



formation of monodentate carbonates and contributes to higher catalytic activity, as confirmed by *operando* FT-IR. Additionally, among LaAlO₃-based catalysts, variations in S_{Ni} play a significant role: larger metallic surface areas correlate with increased catalytic performance, reflecting the positive influence of more Ni⁰ sites at the support-metal interface on H₂ uptake (Tables 1 and 2).

Another relevant aspect when analyzing the influence of Ni loading, beyond its effect on the accessible metallic surface area, is the structure-sensitive nature of the reaction, which is intrinsically linked to the size of Ni⁰ particles. For the 5Ni/LaAlO₃-ex catalyst, for instance, the applied reduction conditions led to substantially smaller Ni⁰ particles (8 nm) compared with the other samples (Fig. 9). This morphological difference contributes to the observed variations in $E_{\text{a,CH}_4}$ and TOF values at 250 °C (Table 2).

The trend indicates that the lower $Y_{250^\circ\text{C}}$ values obtained for 5Ni/LaAlO₃-ex can be attributed to its higher $E_{\text{a,CH}_4}$, which results from the reduced particle size. As the average Ni⁰ particle size increases, the turnover frequency gradually approaches a near-constant regime, indicating that structure-sensitivity becomes more pronounced for particles below approximately 12 nm.

These findings align with the results reported by Varvoutis *et al.*⁷², who demonstrated that Ni⁰ particles smaller than 10 nm diminish the extent of the peripheral interface between the support and step/edge or kink/corner Ni⁰ sites, features recognized as the primary active sites for CO₂ activation. Conversely, particles in the range of 15–20 nm appear to deliver enhanced performance by achieving a balance between interfacial activity and the diminishing effect of excessively large metallic domains.

3.3 Biogas upgrade tests

The catalyst exhibiting the best performance, 15Ni/LaAlO₃, was subsequently evaluated for biogas upgrading to assess its applicability under conditions relevant to practical energy systems. Raw biogas, after purification steps such as desulfurization and drying, typically contains 50–75% CH₄ and 25–50%

CO, with the exact composition depending on the feedstock and anaerobic digestion conditions.⁷⁶

By reacting the CO₂ fraction with H₂ *via* CO₂ methanation, the methane concentration can be significantly increased, while simultaneously valorizing CO₂ as a carbon source and utilizing H₂ from renewable sources.⁷³ This upgrading process enables the production of high-quality renewable fuels, such as bi-methane with CH₄ contents above 90%⁷⁴ or synthetic natural gas (SNG) exceeding 95% CH₄,⁷⁵ which are compatible with existing natural gas infrastructure for storage, transport, and end-use applications.

Enhancing the CH₄ content in this manner increases the energy density of biogas, improving its viability as a renewable energy source and enabling transport *via* existing natural gas infrastructure.^{77,78} To simulate a representative sweetened biogas, a mixture of 60% CH₄ and 40% CO₂ was adopted, reflecting an average biogas composition.

Based on the temperature dependence of CO₂ conversion, 320 °C was selected for the biogas tests, as this temperature lies below the reaction equilibrium, allowing any catalyst deactivation to be detected.

The influence of contact time (τ) was first evaluated by varying the WHSV from 6000 to 43 000 mL (g_{CAT} h)⁻¹ while maintaining a constant inlet flow composition (250 mL min⁻¹; CO₂:H₂:N₂ = 18:72:10). Maximum CO₂ conversion was observed at 10 000 mL (g_{CAT} h)⁻¹, consistent with literature reports showing a plateau in conversion as contact time increases⁷⁹ (Fig. S12).

This behavior likely occurs because, under the applied space velocities, the system operates in a mass-transfer-limited regime. Under such conditions, increasing the contact time beyond a certain threshold does not further enhance the reaction rate, since the transport of reactants to the active sites and the removal of products from these sites are no longer improved.

This WHSV was then applied in long-term biogas stability tests under the conditions described in Section 4.3. CH₄ remained inert, as indicated by identical inlet and outlet flows, confirming the absence of side reactions. The initial CO₂ conversion was 80.0%, slightly lower than the 83.0% observed without CH₄ (Fig. 10), likely due to the reduction in partial pressure caused by CH₄ addition, which affects reaction kinetics.⁸⁰ (Fig. 10).

Despite minor initial deactivation, the material exhibited steady stability over 24 hours, with CO₂ conversion remaining around 75.4%, CH₄ selectivity at 99.6%, and CO being the only detectable byproduct. The carbon balance stayed within $\pm 5\%$, indicating negligible coke formation throughout the experiment.

Based on these results, if the outlet stream is purified to retain only CO₂ and CH₄, feasibly achieved *via* pressure swing adsorption using pore-tailored materials,⁸¹ the resulting gas composition would be CH₄ 90.2%/CO₂ 9.8%, corresponding to an increase of approximately 50.3% in CH₄ content relative to the inlet biogas. As this upgraded stream exceeds 90% CH₄, it qualifies as biomethane according to the thresholds reported by

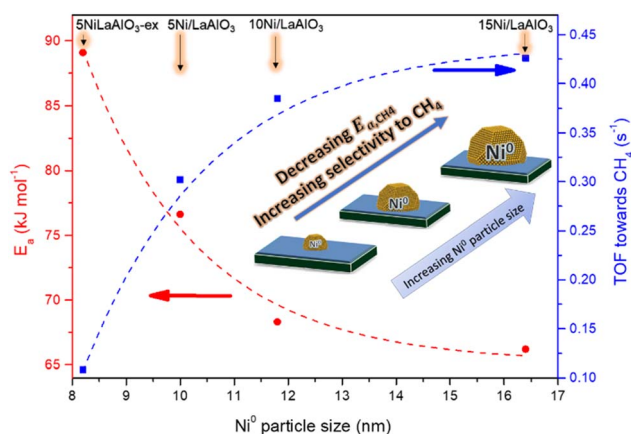


Fig. 9 Relationship between Ni⁰ particle size and the turnover frequency (TOF) for CH₄ formation over the series of LaAlO₃-supported catalysts.



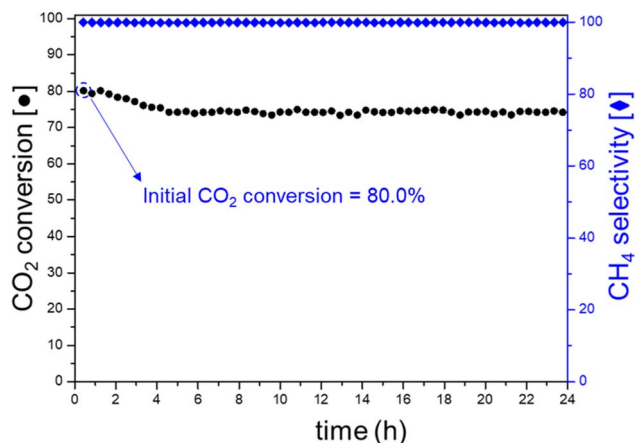


Fig. 10 Time-on-stream evolution of CO₂ conversion (●) and CH₄ selectivity (◆) during the stability test of 15Ni/LaAlO₃-R using a sweetened synthetic biogas feed. Reaction conditions: 320 °C, 1 atm, WHSV = 10 000 mL (g_{cat}·h)⁻¹. Inlet composition: CO₂, H₂, N₂, CH₄ = 45, 180, 25, and 67.5 mL·min⁻¹, respectively.

Kapoor *et al.*,⁷⁴ enabling transport through existing pipeline infrastructure without requiring technological modifications.⁸²

An alternative approach is to retain a fraction of unreacted H₂ in the flow, allowing direct hydrogen to blend into the bi-methane. This strategy has been proposed as a near-term pathway to reduce CO₂ emissions while integrating H₂ produced *via* low-carbon processes such as electrolysis.⁸³

SEM and TEM analyses of the 15Ni/LaAlO₃<ST> catalyst after the stability test (Fig. S13) indicate that the initial deactivation can be attributed to slight metallic sintering. XRD results show an increase in the average Ni⁰ crystallite size from 34 nm (15Ni/LaAlO₃) to 41 nm (15Ni/LaAlO₃<ST>) (Fig. S14), while no NiAl₂O₄ phase formation was detected, and the overall phase composition remained consistent with the post-reduction state. Elemental analysis and microscopy confirmed the absence of carbon deposits, demonstrating that coke formation did not occur under the applied experimental conditions.

4. Conclusions

For the first time, a comparative study of Ni-based catalysts supported on La₂O₃, Al₂O₃, and LaAlO₃, was conducted for the CO₂ methanation reaction. Initial catalytic tests demonstrated that LaAlO₃-based catalysts exhibit a clear metal-oxide synergy, which is rationalized through a multi-technique characterization approach that included H₂-chemisorption, CO₂-TPD-MS, and SEM-TEM analyses.

Despite similar Ni⁰ crystallite sizes and metallic surface areas across the series, LaAlO₃-supported catalysts displayed a markedly higher concentration of moderate basicity sites, which promoted the formation of carbonate species with varying coordination modes. *Operando* FT-IR experiments revealed that monodentate carbonate species anchored on these sites play a central role in the associative CO₂ methanation mechanism, highlighting the positive effect of tuning moderate basicity site concentration on catalytic performance.

Once LaAlO₃ was identified as the most promising support, the influence of Ni loading and preparation method was evaluated. The 15 wt% Ni catalyst prepared by incipient wetness impregnation (15Ni/LaAlO₃) achieved the best performance, attributed to a synergistic combination of favorable Ni reducibility, higher available metallic surface, and formation of monodentate carbonate intermediates at moderate basicity sites. *Operando* FT-IR studies confirmed that the interaction of H-species with these carbonate intermediates drives CH₄ formation *via* the associative mechanism, consistent with the kinetic analysis.

Finally, 15Ni/LaAlO₃ was tested for upgrading a sweetened synthetic biogas (60% CH₄/40% CO₂). Under optimal conditions, 24-hour stability tests at 320 °C achieved high CO₂ conversion ($X_{\text{CO}_2} = 75.4\%$) and CH₄ selectivity ($S_{\text{CH}_4} = 99.6\%$), producing a biomethane mixture with 90.2% CH₄ and 9.8% CO₂. The unreacted H₂ in the outlet stream could potentially be blended into the biomethane, demonstrating the potential of this catalytic system for injection into existing natural gas infrastructure.

Overall, these findings clarify the role of moderate basicity sites in CO₂ methanation and provide mechanistic insight critical for designing more efficient catalysts. Moreover, this study demonstrates the innovative application of LaAlO₃-based catalysts for biogas upgrading, opening avenues for exploring other mixed-oxide supports.

Author contributions

R. B. Machado-Silva: conceptualization; data curation; formal analysis; investigation; validation; visualization; writing – original draft. L. M. Andrés-Olmos: data curation; investigation; writing – review & editing. N. Kosinov: conceptualization; methodology; funding acquisition; writing – review & editing; supervision; validation; visualization. E. J. M. Hensen: conceptualization; methodology; funding acquisition; writing – review & editing; supervision. A. Chica: conceptualization; methodology; funding acquisition; writing – review & editing; supervision; resources.

Conflicts of interest

The authors declare no conflicts of interest.

Data availability

The data supporting this article have been included as part of the supplementary information (SI). Supplementary information is available. See DOI: <https://doi.org/10.1039/d6ta00070c>.

Acknowledgements

We gratefully acknowledge financial support from the Spanish Ministry of Science and Innovation through grants PID2022-139663OB-I00, TED2021-130372B-C44, and CEX2021-001230-S (funded by MCIN/AEI/10.13039/501100011033), as well as from the Generalitat Valenciana (grant CIPROM/2022/10). Raul



Bruno Machado da Silva thanks the “la Caixa” Foundation InPhINIT Program (ID 100010434, fellowship code LCF/BQ/DI19/11730019) for funding his research. We also express our sincere appreciation to the Microscopy Service at the Polytechnic University of Valencia and the technical staff at Eindhoven University of Technology for their essential support in the design and execution of the CO₂-TPD-MS and *operando* FT-IR measurements.

References

- Z. Zuo, Y. Sha, P. Wang and Z. Da, *RSC Adv.*, 2024, **14**, 7468–7489.
- J. Zhang, Z. Wu and F. Polo-Garzon, *ACS Catal.*, 2023, **13**, 15393–15403.
- C. Zhang, F. Wang, B. Xiong and H. Yang, *Nano Converg.*, 2022, **9**, 22.
- T. Zahra, K. S. Ahmad, C. Zequine, R. K. Gupta, A. G. Thomas, M. K. Okla, G. A. Ashraf and M. M. Gul, *Ionics*, 2024, **30**, 3431–3442.
- C. Xu, X. Yang, S. Li, K. Li, B. Xi, Q.-W. Han, Y.-P. Wu, X.-Q. Wu, R.-a. Chi and D.-S. Li, *Inorg. Chem. Front.*, 2023, **10**, 85–92.
- F. J. Perez-Alonso, I. Melián-Cabrera, M. López Granados, F. Kapteijn and J. L. G. Fierro, *J. Catal.*, 2006, **239**, 340–346.
- E. C. Vagia and A. A. Lemonidou, *J. Catal.*, 2010, **269**, 388–396.
- F. R. García-García and I. S. Metcalfe, *Catal. Commun.*, 2021, **160**, 106356.
- W. J. Lee, C. Li, H. Prajitno, J. Yoo, J. Patel, Y. Yang and S. Lim, *Catal. Today*, 2021, **368**, 2–19.
- P. Aieamsam-Aung, A. Srifá, W. Koo-Amornpattana, S. Assabumrungrat, P. Reubroycharoen, P. Suchamalawong, C. Fukuhara and S. Ratchahat, *Sci. Rep.*, 2023, **13**, 9342.
- N. D. M. Ridzuan, M. S. Shaharun, M. A. Anawar and I. Ud-Din, *Catalysts*, 2022, **12**, 469.
- L. Wei, H. Azad, W. Haije, H. Grenman and W. de Jong, *Appl. Catal., B*, 2021, **297**, 120399.
- R. P. Ye, Q. Li, W. Gong, T. Wang, J. J. Razink, L. Lin, Y. Y. Qin, Z. Zhou, H. Adidharma, J. Tang, A. G. Russell, M. Fan and Y. G. Yao, *Appl. Catal., B*, 2020, **268**, 118474.
- A. Karelavic and P. Ruiz, *ACS Catal.*, 2013, **3**, 2799–2812.
- P. Panagiotopoulou, *Appl. Catal., A*, 2017, **542**, 63–70.
- J. Ren, X. Qin, J. Z. Yang, Z. F. Qin, H. L. Guo, J. Y. Lin and Z. Li, *Fuel Process. Technol.*, 2015, **137**, 204–211.
- F. Wang, S. He, H. Chen, B. Wang, L. Zheng, M. Wei, D. G. Evans and X. Duan, *J. Am. Chem. Soc.*, 2016, **138**, 6298–6305.
- W. Wang, M. Nguyen-Quang, D. Mateo, X. Yong, T. Li, H. Xie, W. Chu, C. Pham-Huu, X. Tu and J. Gascon, *ACS Catal.*, 2025, **15**, 10868–10896.
- S. Rahmani, M. Rezaei and F. Meshkani, *J. Ind. Eng. Chem.*, 2014, **20**, 1346–1352.
- W. Li, H. Wang, X. Jiang, J. Zhu, Z. Liu, X. Guo and C. Song, *RSC Adv.*, 2018, **8**, 7651–7669.
- A. Petala and P. Panagiotopoulou, *Appl. Catal., B*, 2018, **224**, 919–927.
- R. B. Machado-Silva, J. F. Da Costa-Serra and A. Chica, *J. Catal.*, 2024, 115609.
- W. Zhen, B. Li, G. Lu and J. Ma, *Chem. Commun.*, 2015, **51**, 1728–1731.
- R. B. Machado-Silva, C. Cerdá-Moreno and A. Chica, *J. CO₂ Util.*, 2025, **102**, 103234.
- C. Cerdá-Moreno, A. Chica, S. Keller, C. Rautenberg and U. Bentrup, *Appl. Catal., B*, 2020, **264**, 118546.
- G. P. Figueredo, R. L. B. A. Medeiros, H. P. Macedo, Â. A. S. de Oliveira, R. M. Braga, J. M. R. Mercury, M. A. F. Melo and D. M. A. Melo, *Int. J. Hydrogen Energy*, 2018, **43**, 11022–11037.
- Y. Kathiraser, W. Thitsartarn, K. Sutthiumporn and S. Kawi, *J. Phys. Chem. C*, 2013, **117**, 8120–8130.
- Y. Sekine, D. Mukai, Y. Murai, S. Tochiya, Y. Izutsu, K. Sekiguchi, N. Hosomura, H. Arai, E. Kikuchi and Y. Sugiura, *Appl. Catal., A*, 2013, **451**, 160–167.
- Y. Ma, P. Su, Y. Ge, F. Wang, R. Xue, Z. Wang and Y. Li, *Catal. Lett.*, 2022, **152**, 2993–3003.
- S. D. Peter, E. Garbowski, V. Perrichon, B. Pommier and M. Primet, *Appl. Catal., A*, 2001, **205**, 147–158.
- Q. Lin, B. Qiao, Y. Huang, L. Li, J. Lin, X. Yan Liu, A. Wang, W. C. Li and T. Zhang, *Chem. Commun.*, 2014, **50**, 2721–2724.
- Q. N. Tran, F. Martinovic, M. Ceretti, S. Esposito, B. Bonelli, W. Paulus, F. Di Renzo, F. A. Deorsola, S. Bensaid and R. Pirone, *Appl. Catal., A*, 2020, **589**, 117304.
- D. Schmider, L. Maier and O. Deutschmann, *Ind. Eng. Chem. Res.*, 2021, **60**, 5792–5805.
- H. Yang, X. Wen, S. Yin, Y. Zhang, C. E. Wu, L. Xu, J. Qiu, X. Hu, L. Xu and M. Chen, *J. Ind. Eng. Chem.*, 2023, **128**, 167–183.
- L. Liu, B. Mezari, N. Kosinov and E. J. M. Hensen, *ACS Catal.*, 2023, **13**, 15730–15745.
- A. Parastaev, V. Muravev, E. H. Osta, T. F. Kimpel, J. F. M. Simons, A. J. F. van Hoof, E. Uslamin, L. Zhang, J. J. C. Struijs, D. B. Burueva, E. V. Pokochueva, K. V. Kovtunov, I. V. Koptuyug, I. J. Villar-Garcia, C. Escudero, T. Altantzis, P. Liu, A. Béché, S. Bals, N. Kosinov and E. J. M. Hensen, *Nat. Catal.*, 2022, **5**, 1051–1060.
- R. B. Machado-Silva, N. Kosinov, E. J. M. Hensen and A. Chica, *Appl. Catal. B Environ. Energy*, 2025, **375**, 125389.
- J. J. Torrez-Herrera, S. A. Korili and A. Gil, *J. Environ. Chem. Eng.*, 2021, **9**, 105298.
- J. F. Da Costa-Serra, A. Miralles-Martínez, B. García-Muñoz, S. Maestro-Cuadrado and A. Chica, *Int. J. Hydrogen Energy*, 2023, **48**, 26518–26525.
- J. J. González, J. F. Da Costa-Serra and A. Chica, *Int. J. Hydrogen Energy*, 2020, **45**, 20568–20581.
- C. H. Bartholomew and R. B. Pannell, *J. Catal.*, 1980, **65**, 390–401.
- O. W. Awe, Y. Zhao, A. Nzihou, D. P. Minh and N. Lyczko, *Waste Biomass Valoriz.*, 2017, **8**, 267–283.
- J. A. Onrubia-Calvo, A. Bermejo-López, S. Pérez-Vázquez, B. Pereda-Ayo, J. A. González-Marcos and J. R. González-Velasco, *Fuel*, 2022, **320**, 123842.



- 44 W. Brockner, C. Ehrhardt and M. Gjikaj, *Thermochim. Acta*, 2007, **456**, 64–68.
- 45 X. Zeng, L. Zhang, G. Zhao, J. Xu, Y. Hang, H. Pang, M. Jie, C. Yan and X. He, *J. Cryst. Growth*, 2004, **271**, 319–324.
- 46 M. Gibert, P. Zubko, R. Scherwitzl, J. Íñiguez and J.-M. Triscone, *Nat. Mater.*, 2012, **11**, 195–198.
- 47 Â. A. S. Oliveira, R. L. B. A. Medeiros, G. P. Figueredo, H. P. Macedo, R. M. Braga, F. V. Maziviero, M. A. F. Melo, D. M. A. Melo and M. M. Vieira, *Int. J. Hydrogen Energy*, 2018, **43**, 9696–9704.
- 48 K. Li, X. Chang, C. Pei, X. Li, S. Chen, X. Zhang, S. Assabumrungrat, Z.-J. Zhao, L. Zeng and J. Gong, *Appl. Catal., B*, 2019, **259**, 118092.
- 49 E. Rytter, Ø. Borg, B. C. Enger and A. Holmen, *J. Catal.*, 2019, **373**, 13–24.
- 50 J. F. da Costa-Serra, C. Cerdá-Moreno and A. Chica, *Appl. Sci.*, 2020, **10**, 5131.
- 51 X. Yuan, T. Pu, M. Gu, M. Zhu and J. Xu, *ACS Catal.*, 2021, **11**, 11966–11972.
- 52 M. Mosinska, W. Maniukiewicz, M. I. Szykowska-Jozwik and P. Mierczynski, *Catalysts*, 2021, **11**, 1174.
- 53 K. Kalantar-zadeh, J. Z. Ou, T. Daeneke, A. Mitchell, T. Sasaki and M. S. Fuhrer, *Appl. Mater. Today*, 2016, **5**, 73–89.
- 54 R. K. Singha, A. Shukla, A. Yadav, L. N. Sivakumar Konathala and R. Bal, *Appl. Catal., B*, 2017, **202**, 473–488.
- 55 M. M. Nair, S. Kaliaguine and F. Kleitz, *ACS Catal.*, 2014, **4**, 3837–3846.
- 56 M. Chen, C. Wang, Y. Wang, Z. Tang, Z. Yang, H. Zhang and J. Wang, *Fuel*, 2019, **247**, 344–355.
- 57 X. Li, D. Li, H. Tian, L. Zeng, Z.-J. Zhao and J. Gong, *Appl. Catal., B*, 2017, **202**, 683–694.
- 58 C. Montero, A. Ochoa, P. Castaño, J. Bilbao and A. G. Gayubo, *J. Catal.*, 2015, **331**, 181–192.
- 59 S. Ewald and O. Hinrichsen, *Appl. Catal., A*, 2019, **580**, 71–80.
- 60 N. Schreiter, J. Kirchner and S. Kureti, *Catal. Commun.*, 2020, **140**, 105988.
- 61 M. Cañón-Alvarado, C. Blanco and C. Daza, *J. Environ. Chem. Eng.*, 2024, **12**, 112224.
- 62 F. Han, Q. Liu, D. Li and J. Ouyang, *J. Environ. Chem. Eng.*, 2023, **11**, 110331.
- 63 C. Sun, K. Świrk Da Costa, Y. Wang, L. Li, M. Fabbiani, V. Hulea, M. Rønning, C. Hu and P. Da Costa, *Fuel*, 2022, **317**, 122829.
- 64 K. N. Ahmad, S. Samidin, M. I. Rosli, M. R. Yusop, M. B. Kassim, B. V. Ayodele, M. A. Yarmo and W. N. R. Wan Isahak, *J. Environ. Chem. Eng.*, 2023, **11**, 111109.
- 65 R. C. Rabelo-Neto, M. P. Almeida, E. B. Silveira, M. Ayala, C. D. Watson, J. Villarreal, D. C. Cronauer, A. J. Kropf, M. Martinelli, F. B. Noronha and G. Jacobs, *Appl. Catal., B*, 2022, **315**, 121533.
- 66 A. Bermejo-López, B. Pereda-Ayo, J. A. Onrubia-Calvo, J. A. González-Marcos and J. R. González-Velasco, *J. Environ. Chem. Eng.*, 2023, **11**, 109401.
- 67 W. K. Fan and M. Tahir, *J. Environ. Chem. Eng.*, 2021, **9**, 105460.
- 68 C. Italiano, J. Llorca, L. Pino, M. Ferraro, V. Antonucci and A. Vita, *Appl. Catal., B*, 2020, **264**, 118494.
- 69 A. Cárdenas-Arenas, A. Quindimil, A. Davó-Quiñero, E. Bailón-García, D. Lozano-Castelló, U. De-La-Torre, B. Pereda-Ayo, J. A. González-Marcos, J. R. González-Velasco and A. Bueno-López, *Appl. Catal., B*, 2020, **265**, 118538.
- 70 M.-X. Huang, F. Liu, C.-C. He, S.-Q. Yang, W.-Y. Chen, L. Ouyang and Y.-J. Zhao, *Chem. Phys. Lett.*, 2021, **768**, 138396.
- 71 A. Quindimil, J. A. Onrubia-Calvo, A. Davó-Quiñero, A. Bermejo-López, E. Bailón-García, B. Pereda-Ayo, D. Lozano-Castelló, J. A. González-Marcos, A. Bueno-López and J. R. González-Velasco, *J. CO2 Util.*, 2022, **57**, 101888.
- 72 G. Varvoutis, M. Lykaki, S. Stefa, V. Binas, G. E. Marnellos and M. Konsolakis, *Appl. Catal., B*, 2021, **297**, 120401.
- 73 F. Bauer, T. Persson, C. Hulteberg and D. Tamm, *Biofuel Bioprod. Biorefining*, 2013, **7**, 499–511.
- 74 R. Kapoor, P. M. V. Subbarao, V. K. Vijay, G. Shah, S. Sahota, D. Singh and M. Verma, *Appl. Energy*, 2017, **208**, 1379–1388.
- 75 S. Szima and C.-C. Cormos, *Energies*, 2021, **14**, 1258.
- 76 Y. Li, C. P. Alaimo, M. Kim, N. Y. Kado, J. Peppers, J. Xue, C. Wan, P. G. Green, R. Zhang, B. M. Jenkins, C. F. A. Vogel, S. Wuertz, T. M. Young and M. J. Kleeman, *Environ. Sci. Technol.*, 2019, **53**, 11569–11579.
- 77 M. A. A. Aziz, A. A. Jalil, S. Triwahyono and A. Ahmad, *Green Chem.*, 2015, **17**, 2647–2663.
- 78 C. Vogt, M. Monai, G. J. Kramer and B. M. Weckhuysen, *Nat. Catal.*, 2019, **2**, 188–197.
- 79 L. Failing, P. Strucks and S. Kaluza, *Chem. Ing. Tech.*, 2023, **95**, 749–753.
- 80 T. Burger, P. Donaubauber and O. Hinrichsen, *Appl. Catal., B*, 2021, **282**, 119408.
- 81 J. Shang, A. Hanif, G. Li, G. Xiao, J. Z. Liu, P. Xiao and P. A. Webley, *Ind. Eng. Chem. Res.*, 2020, **59**, 7857–7865.
- 82 M. Calero, V. Godoy, C. G. Heras, E. Lozano, S. Arjandas and M. A. Martín-Lara, *Sustain. Energy Fuels*, 2023, **7**, 3584–3602.
- 83 S. Pellegrino, A. Lanzini and P. Leone, *Renew. Sustain. Energy Rev.*, 2017, **70**, 266–286.

